Three-Dimensional Image Inpainting System Using 3D-ED-GAN for Efficient Vision-Based Detection for Rotor Dynamic Balance System

YI-HAO CHUNG AND YEN-LIN CHEN, (Senior Member, IEEE)

Department of Computer Science and Information Engineering, National Taipei University of Technology, Taipei 10608, Taiwan

Corresponding author: Yen-Lin Chen (ylchen@mail.ntut.edu.tw)

ABSTRACT We propose a three-dimensional (3D) image inpainting system using the 3D encoder–decoder generative adversarial network (IISU3EDGAN) for providing accurate detection results in vision-based rotor dynamic balancing processes. The proposed IISU3EDGAN system integrates 3D sensors with a deep learning network to reconstruct corrupted rotor images, thereby optimizing the detection parameters. In rotor component detection processes, overexposed images caused by reflections of the metallic rotor shaft affect the accuracy and performance of vision-based inspection systems. Traditional image restoration technologies or inpainting methods are inadequate for solving this problem. By contrast, our proposed system can repair 3D overexposed images of rotors. Compared with traditional image processing methods, the proposed system can adequately manage the complexity of corrupted images. In addition, it can be used to process complex overexposed rotor images and maintain image details. The proposed system can be applied to a wider range of rotor types, and it can be used to optimize the parameters of vision-based rotor detection systems to improve the accuracy of rotor component detection. We conducted experiments and observed that by using 3D sensors and deep learning, the proposed system improved the success rate in the first round of rotor dynamic balancing, reduced the number of rounds required for balancing, and increased the rotor production output. These results thus indicate that the IISU3EDGAN system is applicable and robust and that it can be used to improve the overall efficiency of dynamic balancing on rotor production lines.

INDEX TERMS Dynamic balancing, 3D sensor, GAN, image inpainting, manufacturing automation, rotor.

I. INTRODUCTION

Motor technology is extensively used in diverse applications, including heavy industrial equipment and small toys. The rotor of a motor may be affected by the centrifugal force engendered by rotational eccentricity. Therefore, the dynamic balancing of rotors is crucial. ISO 1940-1:2003 [1] specifies 11 balance quality grades for a rotor during rotation. If a rotor exceeds the specified imbalance tolerance, it causes vibration and noise and may even cause machine malfunction. Accordingly, rotor balance [2] is a critical consideration in motor manufacturing processes.

Several factors contribute to rotor imbalance, including uneven rotor materials, unbalanced couplings, and rotor machining errors. Rotor imbalance can be divided into two primary categories: static and dynamic [3]. In motor manufacturing, the field balancing method is widely used to correct dynamic imbalance [4]. In this method, a dynamic balancing machine is used to measure and acquire rotor vibration data, in addition to calculating the imbalance angle and magnitude to provide rotor balancing instructions to an operator. Dynamic balancing machines can be classified into two categories according to the mechanism through which the rotor is supported on pedestals: hard-bearing and soft-bearing machines [4]. In soft-bearing machines, the rotor suspension vibrates during a rotation test. The frequency and amplitude of this imbalanced vibration can be measured

The associate editor coordinating the review of this manuscript and approving it for publication was Huiyan Zhang.

using a vibration sensor, and the dynamic imbalance can be corrected to be within the allowable range.

Numerous dynamic balancing strategies and methods have been proposed over the years. By considering both residual vibration and correction mass as performance function parameters, Fujisawa *et al.* [5] proposed an improved balancing method that reduces the magnitude of the correction masses. To reduce the imbalance of a high-speed spindle system, Zhang *et al.* [6] developed an automatically controlled pneumatic online dynamic balance system. Zhao *et al.* [7] proposed a transient characteristic–based balancing method (TCBM) in combination with a dynamic load identification (DLI) technique for identifying the imbalance parameters of a general rotor system. Green *et al.* [8] performed a nonlinear bifurcation analysis of the dynamics of an automatic dynamic balancing mechanism for rotating machines. They deployed two or more masses that could freely travel around a race at a fixed distance from the hub and could then balance any eccentricity in the rotor. In [9], an adaptive imbalance control method for active magnetic bearings, called generalized notch filter, was proposed to increase the efficiency of dynamic balancing; this method was used to restrain the synchronous vibration of a rotor and identify the distribution of rotor imbalance, and it was applied to decrease the vibration amplitude. By utilizing multisensor fusion instead of a single sensor, Liu and Qu [10] proposed a holo-balancing method for rotor systems; specifically, they successfully applied the holospectral principle to traditional balancing methods for flexible rotor systems.

Ostlund and Brokemper [11] presented a digital control algorithm based on rotor saliency under no load for detecting the initial rotor position in order to estimate the rotor position. Schmidt *et al.* [12] presented a technique for calculating the absolute angular position of a permanent magnet rotor by selecting an appropriate voltage pulse width and applying it to each phase winding to discern the absolute rotor position. Jansen and Lorenz [13] tracked the magnetic saliency of rotors through the injection of an inverter-generated balanced three-phase high-frequency signal, followed by the execution of appropriate signal demodulation and processing combined with a closed-loop observer. Degner and Lorenz [14] analyzed the effects of multiple spatial harmonic saliencies on the estimation of flux angle, position, and velocity; they also presented methods entailing the use of multiple spatial harmonic saliencies to provide wide-bandwidth and highly accurate estimates of flux angle, rotor position, and velocity. However, applying the field balancing method in a rotor factory would require individual rotors to be positioned on the balancing machine before they can be assembled with stators.

In the field balancing method, a balancing machine rotates a rotor to measure the angle of imbalance and magnitude of the imbalance vector. Before a dynamic balancing machine rotates a rotor, the position of the key phasor (KP) must be marked—with the shaft sleeve serving as the reference position—so that the dynamic balancing machine can calculate the rotation phase and speed. After the dynamic balancing machine calculates the imbalance vector, the operator mounts washers of a specific weight at the specific balance sprue (BS) positions to offset the imbalance vector. Fig. 1 illustrates the positions of the KP, BS, and different types of rotors. Operator experience determines the number of operation rounds required for dynamic balancing, which affects the production capacity of motors and introduces uncertainty in dynamic balancing. For human operators, completing the dynamic balancing process in a single round is difficult, which engenders redundant dynamic balancing rounds. This not only increases the processing time of dynamic balancing and reduces the production capacity but also increases the wear and tear of the balancing machine.

To address the uncertainty of human judgment, Chung and Chen [15], [16] have proposed an adaptive vision-based method (AVBM) that uses three-dimensional (3D) time-of-flight (ToF) sensors [17] to capture 3D images of the rotor, followed by the use of depth and amplitude data fusion technology [18] for pattern recognition. The ToF camera works by illuminating the target with a modulated light source and observing the reflected light. The depth engine generates a 3D point cloud by calculating the phase shifts between the illumination and reflection [19]. Fig. 2 illustrates the concept of the ToF sensor. Through the use of fusion technology, the AVBM can accurately detect the center position of the KP and the angles between the KP and BS. In summary, this method analyzes the imbalance vector and determines the optimal washer installation configuration, which considerably reduces the number of redundant rounds in existing dynamic balancing process. Nevertheless, during the process of capturing two-dimensional (2D) rotor amplitude and 3D rotor depth images, overexposed rotor images cause detection errors, thus reducing the robustness of the AVBM.

To compensate for overexposed 2D images in vision-based methods, studies have proposed various methods. Guo *et al.* [20] introduced an overexposure correction method based on an overexposure likelihood; in this method, the color of each overexposed pixel is corrected through neighborhood propagation, and the correction is based on the confidence of the original color. Lee *et al.* [21] combined an overexposure correction method with lightness correction and chrominance restoration. They corrected lightness by retaining a 2D Gaussian function model and preserving the gradients of the original lightness. Moreover, they predicted the color of the overexposed areas by propagating the stretched color of the neighboring non-overexposed region. Zhang *et al.* [22] proposed an automatic exposure correction method that separately achieves underexposure and overexposure correction by estimating the illumination of the input image and inverted input image. Through dual illumination estimation and multiexposure image fusion, a globally well-exposed image can be adaptively obtained by blending two intermediate exposure correction images with the input image. In addition to the aforementioned overexposure repair methods for color images, Huang *et al.* [23] repaired overexposed computed tomography images by using a mixed one-bit

compressive sensing (M1bit-CS) technique, which acquires information from both regular and saturated measurements. However, overexposed grayscale amplitude images of rotors are severely corrupted, and the aforementioned image correction technique cannot completely repair the corrupted areas. In our previous study [24], we leveraged the alignment between 3D depth and 2D amplitude images to detect overexposed areas by using 3D depth data; we repaired the 2D amplitude image by using the mean value of nonoverexposed amplitude image pixels. However, differences in rotor types and the complexity of overexposed images engender challenges in our method. To improve rotor detection accuracy, one can adopt deep learning models to effectively overcome the complexity of overexposed rotor images and directly compensate for overexposed 3D depth images.

Effective deep learning methods for image restoration include generative adversarial network (GAN) methods that are based on deep learning networks. A GAN is an unsupervised learning model proposed by Goodfellow *et al.* [25] in 2014. It is composed of a generator and a discriminator. The generator outputs the predicted data, and the discriminator distinguishes whether the predicted data are true. On the basis of the mutual confrontation of the generator and discriminator, predictions provided by the generator are expected to be hardly distinguished by the discriminator. Denton *et al.* [26] introduced a generative parametric model that applies a cascade of convolutional networks within a Laplacian pyramid framework to generate high-quality samples of natural images in a coarse-to-fine fashion. Radford *et al.* [27] proposed a class of convolutional neural networks (CNNs) called deep convolutional generative adversarial networks (DCGANs) and demonstrated that a pair of DCGANs can learn a hierarchy of representations from object parts to scenes in both the generator and discriminator.

In recent years, 3D computer-aided design datasets [28], [29] have been used to develop a new data-driven approach for 3D generative modeling. Achlioptas *et al.* [30] introduced a deep autoencoder network with state-of-the-art reconstruction quality and generalization ability. By focusing on the generator in a GAN and defining a graph convolution method, Valsesia *et al.* [31] studied the unsupervised problem of a generative model by using exploiting graph convolution. Yan *et al.* [32] investigated an encoder–decoder (ED) network that considers projection transformation as regularization. Girdhar *et al.* [33] proposed the TL-embedding network architecture consisting of an autoencoder and a convolutional network to learn an embedding space. Wu *et al.* [34] introduced a 3D GAN by leveraging a volumetric convolutional network and generative adversarial nets.

Studies have developed several GAN extension methods for repairing 3D data. Pathak *et al.* [35] presented context encoders based on a CNN that was trained to generate the content of an arbitrary image region conditioned on its surroundings. Wang *et al.* [36] proposed a 3D mesh repair method based on a 3D deep convolutional GAN composed of a local GAN and a global GAN. The two GANs can generate the

repaired area while maintaining the details of the region. Dai *et al.* [37] introduced a 3D encoder–predictor network composed of 3D convolutional layers for predicting and filling in missing data. Yu *et al.* [38] developed a point encoder GAN that can process point cloud data directly without any labeling or assumptions. This method applies a max-pooling layer and two T-nets [39] to ensure a suitable feature representation of the point cloud. By using a novel 3D-RecGAN, Yang *et al.* [40] reconstructed the complete 3D structure of a given object from a single depth view. Wang *et al.* [41] proposed a hybrid framework combining a 3D-ED-GAN and a long-term recurrent convolutional network to capture the global contextual structure and localize fine-grained details.

Balancing machines implemented in factories use photoelectric mark sensors to detect the KP position for rotor position detection. By detecting the position of the marker on the rotor shaft sleeve, these machines can calculate the rotor center and KP angle. However, slippage of the rotor rotation belt reduces the accuracy of the derived KP angle. Moreover, photoelectric mark sensors detect only the KP position but not the BS position. Accordingly, this study proposes a 3D-vision-based system for rotor position detection and for repairing overexposed 3D images. Our previously proposed depth-information-based image restoration method for rotors [24] can reconstruct 2D amplitude data of the rotor shaft; however, the 3D depth data of the rotor shaft must be further processed to accurately detect the KP angle. Therefore, a deep-learning-based 3D-ED-GAN can be used to solve this problem. Our previous study presented a preliminary 3D image inpainting method for rotors, but we applied the method for low-resolution image inpainting. To accurately detect the KP center position by using 3D depth data, a high-resolution image inpainting method can provide high-integrity 3D images. Hence, the present study proposes a 3D image inpainting system using 3D-ED-GAN(IISU3EDGAN), which can efficiently correct overexposed 3D rotor images, thereby increasing the accuracy of visual rotor detection and improving the production efficiency of dynamic balancing. By processing 3D voxels directly, the proposed system can efficiently process complex overexposed rotor images and significantly improve the accuracy of rotor detection.

The main contributions of this paper are outlined as follows:

1) We present an efficient deep learning GAN for optimal image restoration.
2) Compared with the 2D image repair method in [24] and low-resolution deep learning method in [42], the proposed method facilitates the direct inpainting of high-resolution 3D depth data.
3) The proposed method can overcome the problem of inpainting complex overexposed images with different types of rotors in production lines.
4) The proposed method can substantially improve the production efficiency of actual motor production lines.

The remainder of this paper is organized as follows. Section II provides the problem statement. Section III presents the proposed system. Section IV presents the experimental results and discussions. Finally, Section V concludes this paper.
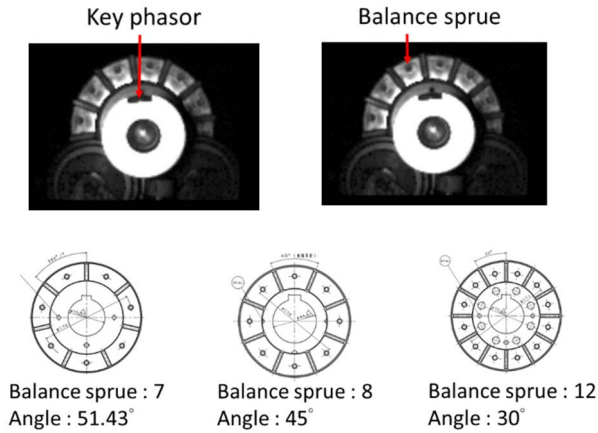

Key phasor   Balance sprue

Balance sprue : 7   Balance sprue : 8   Balance sprue : 12
Angle : 51.43°   Angle : 45°   Angle : 30°

FIGURE 1. KP and BP of a rotor.

pulsed source

reflection

RAW data

Depth engine [ToF = 2d/C]

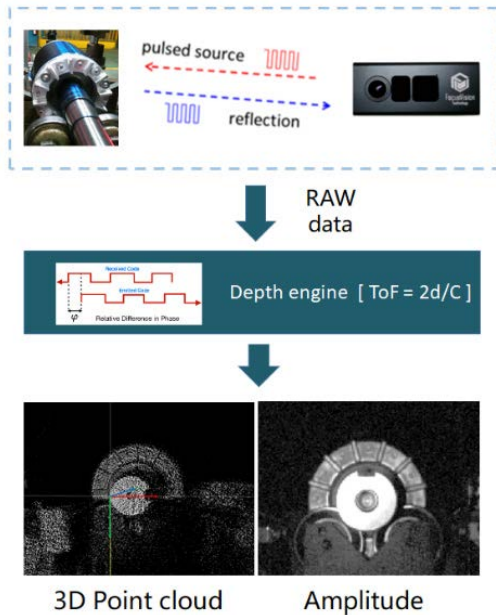3D Point cloud   Amplitude

FIGURE 2. Concept of ToF sensor.

II. PROBLEM STATEMENT

The IISU3EDGAN system for rotor dynamic balancing uses two 3D sensors to obtain 3D images of the left and right sides of a rotor. The 3D sensors are placed vertically at a specific distance from the rotor shafts and face the shafts; the lenses are aligned vertically with the center of the rotor shaft to obtain images of various regions, including the rotor shaft plane and the BSs. Fig. 3 presents a schematic of the arrangement of the rotor and 3D sensors. The dynamic

balancing process in the IISU3EDGAN system involves the following steps: 3D image grabbing, rotor component recognition, imbalance vector analysis, and balance configuration optimization. By using the optimized washer and BS configuration recommendations, the operator can effectively reduce the number of redundant balancing rounds, thus increasing the overall rotor manufacturing productivity. In the 3D rotor image recognition process, the rotor components, including the positions of the shaft center, KP center, and BS positions, must be recognized. Fig. 4 illustrates the plane figure for rotor component detection. The IISU3EDGAN system accurately calculates the angle θ_p between the KP position P and the BS position B_1 on the basis of the positions of these rotor components. After the dynamic balancing machine calculates the imbalance vector $\mathbf{V}$ with angle θ_v, the IISU3EDGAN system uses the angles θ_{b4} and θ_{b5} between the BS and $\mathbf{V}$ to calculate the vector components on B_4 and B_5, after which it generates the optimized configurations for dynamic balancing.

Rotor image overexposure constitutes the most common problem associated with the detection of KP positions through 3D vision. A 3D sensor actively emits infrared light, which leads to the generation of overexposed images owing to reflections from the surface of the rotor's metal shaft. Fig. 5 illustrates various overexposed 3D rotor images. The distribution of the overexposed areas in these images varies with the rotor type. Overexposed images have a unique feature in that the depth data in overexposed areas exceed the unambiguous range of the 3D images; therefore, the AVBM leverages this feature to repair the corresponding 2D amplitude images. In addition, the types of rotors on production lines are rather different. This leads to incomplete 2D image restoration owing to the complexity of the overexposure, which affects the accuracy of KP position detection. Our proposed IISU3EDGAN system can reconstruct overexposed 3D images of rotors, which effectively helps to negate the effects of differences in rotor types and helps repair complex overexposed images. Fig. 6 illustrates the architecture of the proposed IISU3EDGAN system for dynamic balancing. Because this system was designed with the aim of directly repairing 3D images, it improves the accuracy of rotor center detection and KP center point detection, thus improving the overall performance of the dynamic balancing process.

III. 3D IMAGE INPAINTING USING 3D-ED-GAN

The traditional image inpainting method is inadequate for managing the complexity arising from different rotor types on a production line. Deep-learning-based 3D-ED-GAN algorithms provide an effective solution in this scenario. Accordingly, we developed our proposed IISU3EDGAN system with the primary objective of reconstructing overexposed 3D images of a rotor shaft and improving the rotor detection accuracy, thereby improving the efficiency of rotor dynamic balancing. The operating process is described as follows. First, 3D-ED-GAN training can be performed by preparing overexposed and ground-truth 3D voxel datasets. Second, the discriminator model can be trained to distinguish simulated
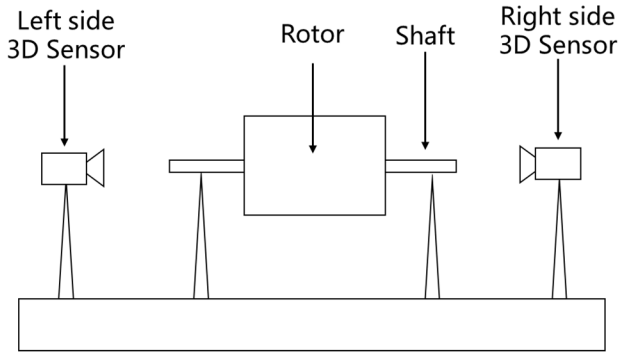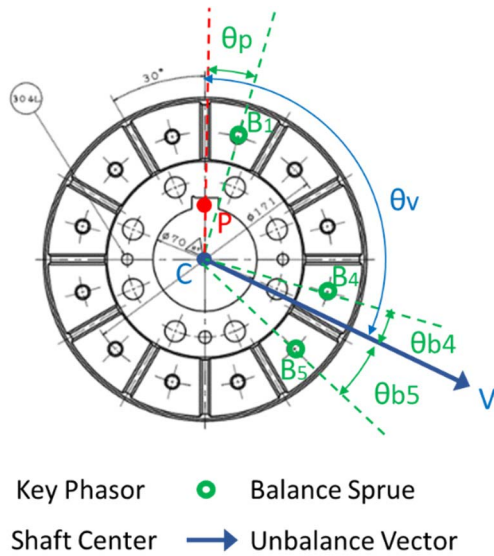
FIGURE 3. Arrangement of rotor and 3D sensor.

FIGURE 4. Plane figure for rotor component detection.
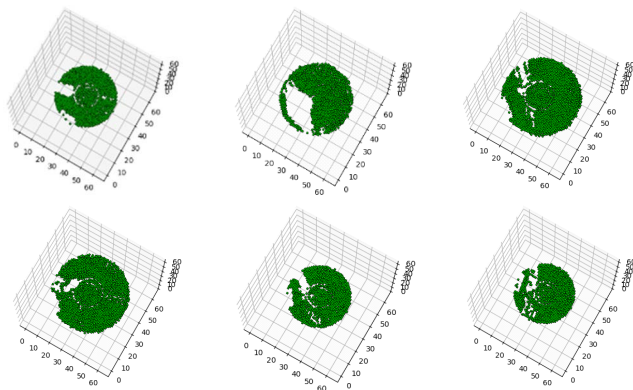

FIGURE 5. Images of overexposed 3D voxel of a rotor.

images and improve the ability of the generator model to fool the discriminator model. Finally, the combined model can be used to predict the 3D voxel that can maintain the integrity of the rotor shaft image. The repaired image can then be used

for subsequent rotor component position detection and rotor dynamic balancing.

A. DATASET AND TRAINING PROCESS

To prepare the rotor dataset for 3D-ED-GAN training in this study, 3D ToF sensors installed on the left and right sides of the rotor were used to capture 3D depth data and 2D amplitude images of the rotor. The 3D depth data were then normalized to the size of $64 \times 64 \times 64$ and converted to the 3D voxel format. We applied a matting spray on the rotor shaft to eliminate metal reflections and obtain nonoverexposed rotor images. Moreover, we prepared an overexposed rotor image dataset and a ground-truth rotor image dataset without overexposure. The training process is described as follows (Fig. 7):

1) Overexposed and ground-truth datasets were prepared before training.
2) The 3D point cloud data were prepared and normalized to the 3D voxel format.
3) The ground-truth and predicted voxels were used to train the discriminator.
4) The combined generator and discriminator model was also trained.
5) The combined model was used to predict 3D voxels.

The repaired 3D voxels predicted using the combined model were reviewed to check whether they fulfilled the system criteria. If they did not meet the criteria, Steps 3–5 of the training process were repeated until the predicted voxels fulfilled the criteria.

B. STRUCTURE OF 3D-ED-GAN

The 3D-ED-GAN algorithm is composed of a generator and a discriminator. The generator is composed of an ED pair. Fig. 8 illustrates the structure of the 3D-ED-GAN algorithm. The encoder transfers the $64 \times 64 \times 64$ 3D voxels into a probabilistic latent space, and the decoder generates the predicted voxel from the latent feature representation. The discriminator classifies whether the predicted voxel is true or false. Through contextual and adversarial loss minimization, the 3D-ED-GAN algorithm can be trained to generate inpainted 3D voxels and contextual consistency can be preserved.

C. GENERATOR AND DISCRIMINATOR OF 3D-ED-GAN

The 3D-ED-GAN algorithm consists of three convolutional networks, namely an encoder, a decoder, and a discriminator. Fig. 9 illustrates the architecture of the 3D-ED-GAN algorithm. The generator accepts overexposed data as the input and generates predicted images by using the 3D encoder and 3D decoder. The 3D encoder, which consists of four 3D convolutional layers (Conv3D) of kernel size $3 \times 3 \times 3$ and stride 2, takes the corrupted 3D voxels of size $64 \times 64 \times 64$ as the input. Each Conv3D layer contains 64, 128, 256, and 512 filters, separately, and these layers use a rectified linear unit (ReLU) as the activation function. The tensor is then calculated using four 3D deconvolution layers (Deconv3D), which constitute a 3D decoder. Each Deconv3D
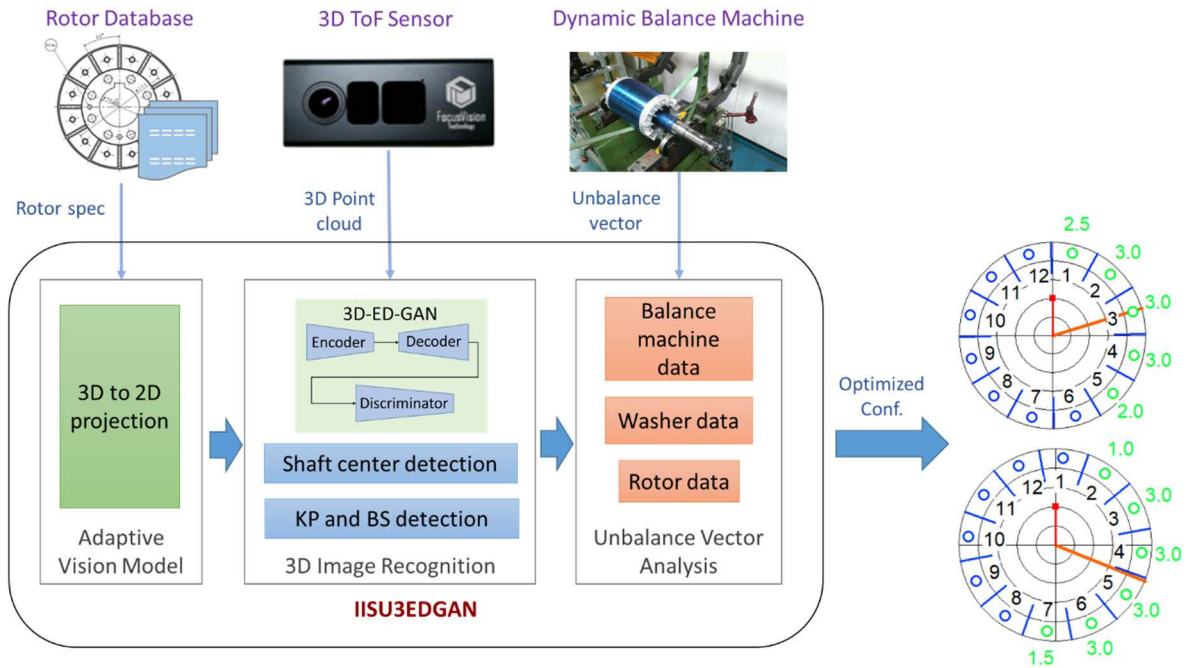
FIGURE 6. Architecture of IISU3EDGAN for rotor dynamic balancing.

contains 512, 256, 128, and 64 filters, separately, of kernel size $3 \times 3 \times 3$ and stride 2. The activation function of the first three layers is ReLU, and that of the last layer is tanh. The discriminator and 3D Encoder have the same architecture; that is, they take the predicted and ground-truth voxels as inputs. The discriminator contains four Conv3D layers, and its activation function is ReLU; the sizes of the core and stride are the same as those in the 3D encoder. Finally, the discriminator ends with a flatten layer and a dense layer that use sigmoid function as the cross-entropy function.

IV. EXPERIMENTAL RESULTS

The proposed IISU3EDGAN system was validated on the production line of TECO Co., Ltd. [43]. We executed our rotor dynamic balancing test by using a dynamic balancing machine manufactured by Nan Jung Electronic Co., Ltd. [44], as illustrated in Fig. 10. We used RL100Pro 3D sensors manufactured by FocusVision Technology Co., Ltd. in our experiments [45]. Table 1 presents a summary of the sensor specifications. The training platform for our experiments was a computer equipped with an Nvidia GeForce GTX 1080Ti graphics processing unit and running Ubuntu 16.04 with Python 3.6.8, Keras 2.2.0, and TensorFlow 1.14.0 (TABLE 2). We acquired 3D data of the rotor shaft and applied the 3D-ED-GAN algorithm to repair overexposed rotor images. The rotor shaft center, radius, KP center position, balance fin, and BS position were detected using the 3D depth data and 2D amplitude data of the rotor, as displayed in Fig. 11. By using the detected information and the imbalance vector provided by the balancing machine, we computed the optimized balance configuration, as shown in Fig. 12.
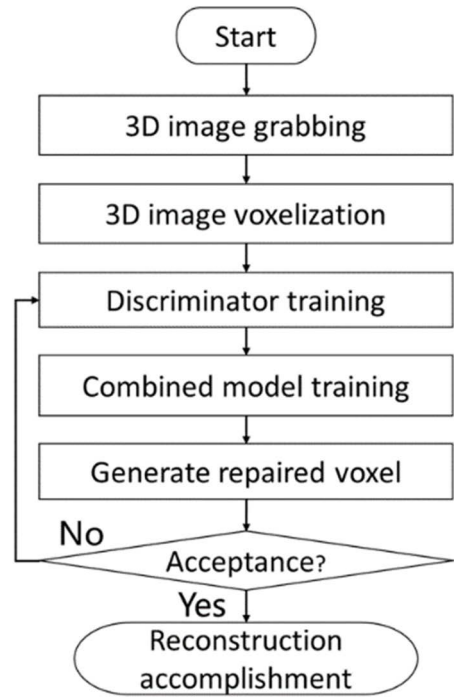

FIGURE 7. Training the 3D-ED-GAN.

We scanned 20 different rotor models with five different sizes to prepare the 3D-ED-GAN training dataset. This dataset was composed of 12 000 3D images. Rotor images derived for each size were divided into training images and
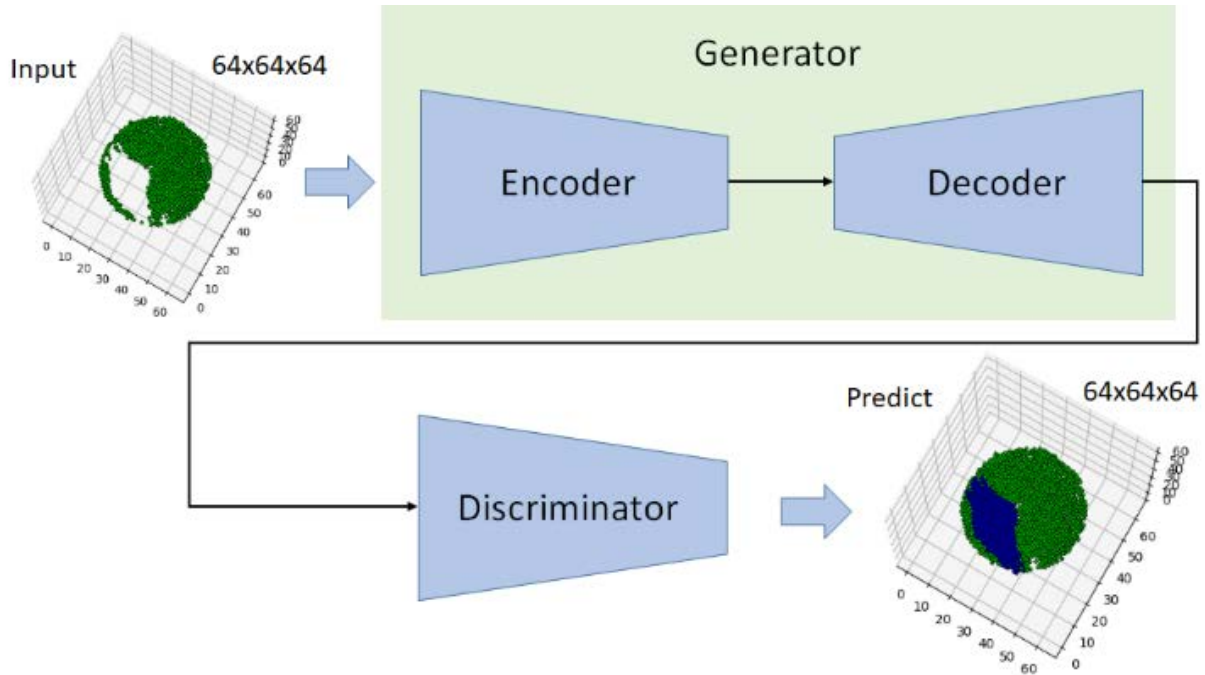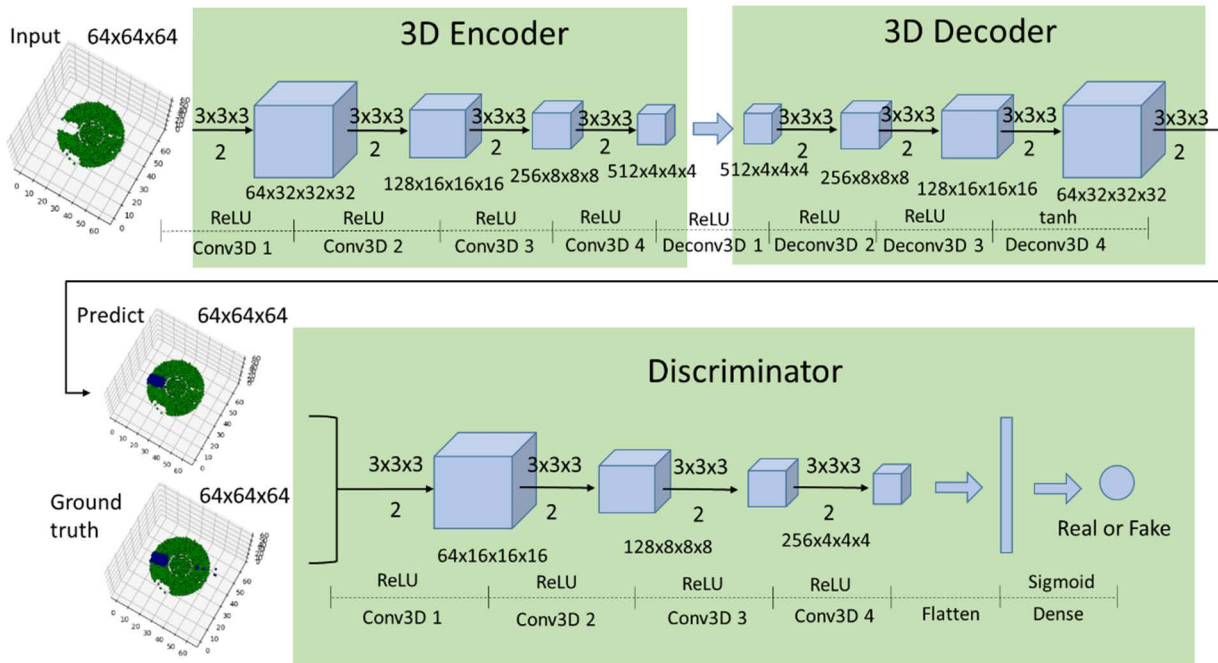
FIGURE 8. Structure of 3D-ED-GAN.

FIGURE 9. Architecture of proposed 3D-ED-GAN.

test images at a ratio of 4:1, resulting in 9600 training images and 2400 test images. Each scan contained overexposed and nonoverexposed ground-truth images. The dataset was voxelized into a 64^3 grid file format. To evaluate the experimental results, we first reviewed the 3D-ED-GAN image inpainting results. Subsequently, we selected two rotors from each of the five rotor size groups (i.e., 10 rotors in total) as the test samples for comparing the AVBM with the IISU3EDGAN system in terms of rotor component detection. Finally, we evaluated the performance of the IISU3EDGAN system in rotor KP angle detection as well as its overall performance in rotor dynamic balancing.

FIGURE 10. Dynamic balancing machine for IISU3EDGAN.

TABLE 1. 3D Sensor specifications.

Model : RL100 Pro	
Dimension	102.1 x 43.5 x 33 mm
Range	0.5 ~ 6 m (up to 13m)
Resolution (Depth / RGB)	320 x 240 / 4Mp
Frame rate	Max 120 fps
FOV (H x V) (Depth / RGB)	74.4 x 57.9 / 110 x 62
Illumination	850 nm, VCSEL
Depth error rate	0.5 %

TABLE 2. Training platform for IISU3EDGAN.

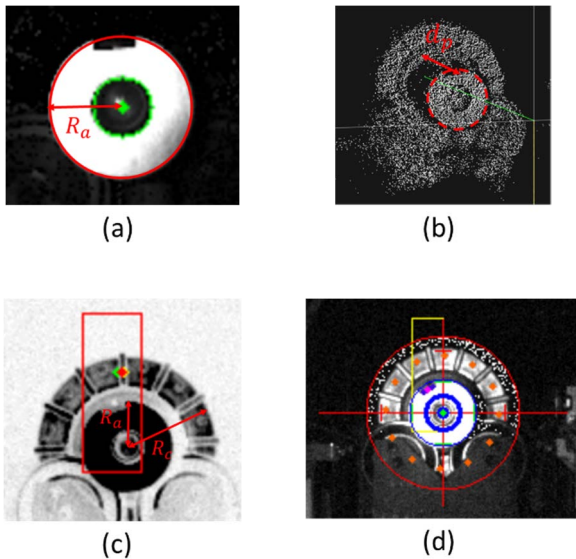| OS	Python	Keras	TensorFlow	GPU
Ubuntu 16.04	3.6.8	2.2.0	1.14.0	Nvidia GeForce GTX 1080Ti

FIGURE 11. Rotor component detection: (a) shaft center and radius, (b) KP center, (c) balance fin, And (d) BS positions.

A. 3D IMAGE INPAINTING
We used 2400 3D scan images obtained using 20 different rotor models of five different sizes as the test data. We derived the mean square error (MSE) and peak signal-to-noise ratio (PSNR) as performance metrics to evaluate the
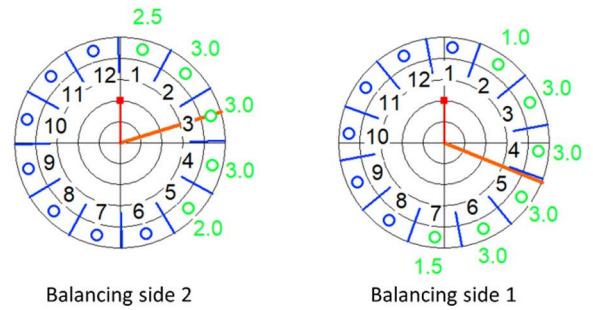
FIGURE 12. Optimized balancing configuration.

FIGURE 13. Training convergence curves of different rotor models.

(a) Average mean square error

(b) Average PSNR

FIGURE 14. 3D image inpainting quality evaluation: (a) average mean square error and (b) average PSNR.

performance of the 3D-ED-GAN algorithm. The equation of MSE for 3D models is expressed in (1):

$$\text{MSE} = \frac{1}{N_{width} \times N_{hight} \times N_{depth}}$$

| Input voxel | Ground truth | Inpainted voxel |

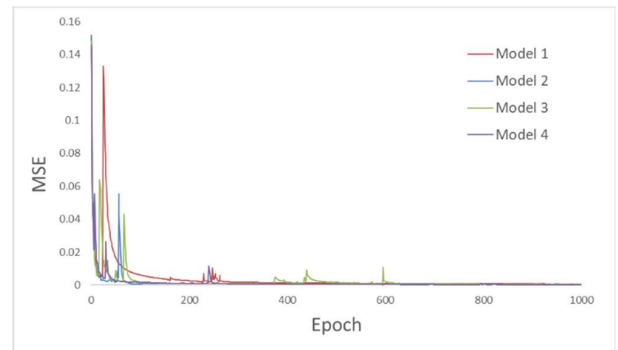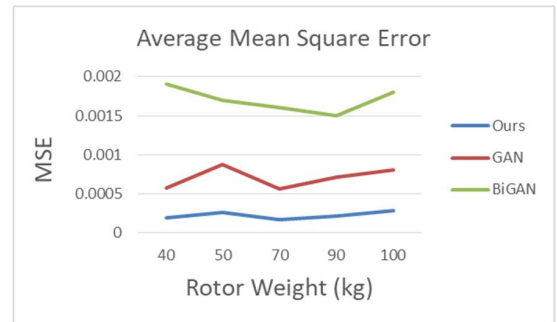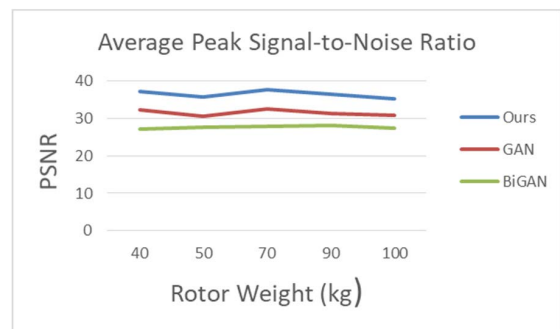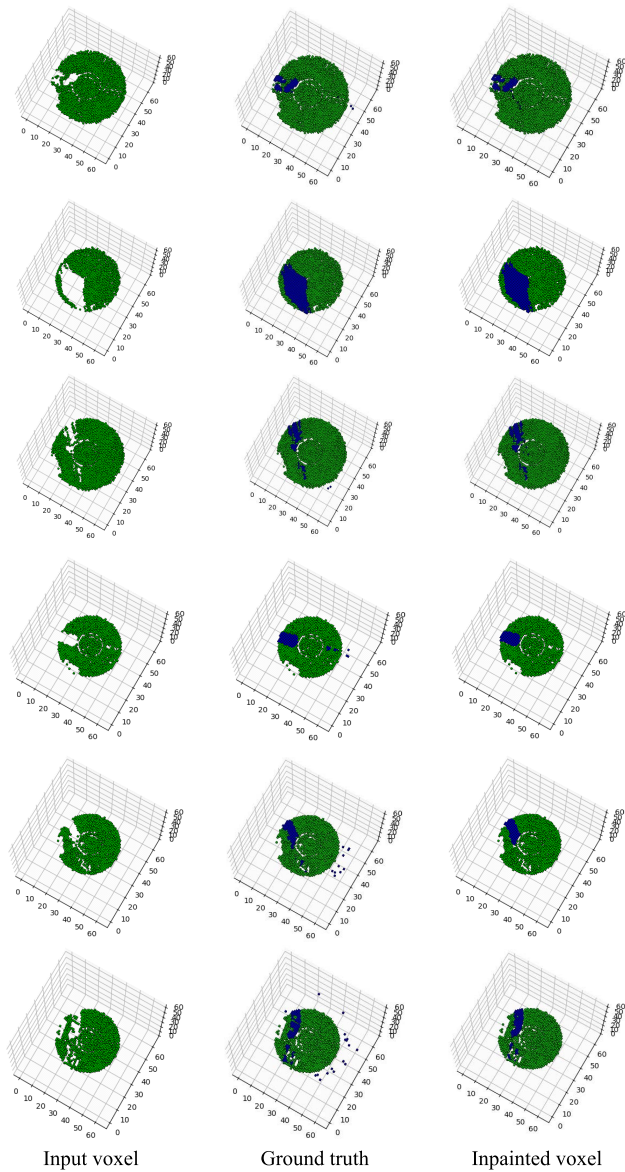**FIGURE 15.** Results of 3D image inpainting.

$$\times \sum_{x=0}^{N_{width}-1} \sum_{v=0}^{N_{hight}-1} \sum_{z=0}^{\sum_{depth}-1} (f(x,y,z)$$
$$- \hat{f}(x,y,z))^2 \qquad (1)$$

where N_{width}, N_{height}, and N_{depth} denote the numbers of pixels in the three dimensions, respectively. $f(x,y,z)$ represents the ground-truth 3D voxels, and $\hat{f}(x,y,z)$ denotes the inpainted 3D voxels. The MSE indicates the difference between the ground-truth and inpainted data.

The PSNR can be defined as follows:

$$PSNR = 20 \times \log_{10} \left(\frac{I_{max}}{\sqrt{MSE}} \right) \qquad (2)$$

where I_{max} can be set to 1 because the 3D voxel grid is a (0, 1) sparse matrix. *PSNR* is an indicator of the degree of distortion. A higher *PSNR* indicates superior image restoration.

We calculated MSE values for four different rotor models, and Fig. 13 presents the training convergence curve obtained using the proposed system. The MSE values derived for models 1 and 2 initially tended to diverge with a few oscillations at approximately 250 epochs. The MSE values for model 3 also oscillated at approximately 600 epochs. However, the values for all rotor models subsequently converged steadily over time. Moreover, we compared the performance of the proposed system with that of GAN [25] and BiGAN [46] algorithms. The average MSE and PSNR were calculated for rotors of five sizes. Fig. 14 displays the comparison results. According to the curves of the average MSE and PSNR, the proposed system had the lowest MSE and the highest PSNR. These results prove that the results obtained using the proposed method were the closest to the ground-truth data.

To repair overexposed rotor images, we voxelized 3D images into 64 × 64 × 64 3D grids as the test data to compare the overexposed images, ground-truth images, and inpainted images. Fig. 15 illustrates the image inpainting results obtained using the proposed system for rotor shafts of different sizes at the same distance. According to the input voxel column, the overexposed areas created holes in the input voxels, and the exposure area occupied nearly one-third of the shaft area. In the figure, the ground-truth column represents unexposed rotor 3D voxels, and the blue area represents overexposed pixels. The inpainted voxel column presents the results obtained using the 3D-ED-GAN algorithm. The results revealed that the 3D-ED-GAN algorithm could restore 3D voxels with different overexposed ranges and areas. According to these results, the proposed system can accurately generate repaired 3D voxels without affecting the KP data. This is helpful for detecting the KP center and BS positions. The proposed system performs well in terms of repairing overexposed areas in different positions and ranges.

B. ROTOR DETECTION EVALUATION

We selected two rotors from each of the five rotor size groups, resulting in a total of 10 rotors, as the test sample. Subsequently, we conducted two rounds of testing (with 10 rotors being used in each round) for the left and right sides of the rotor shafts. We detected the angle between the rotor KP and BS positions after repairing the overexposed rotor images by using the AVBM and IISU3EDGAN system. We detected and calculated the angle between the KP and the nearest BS, recorded the deviations between the detected angles and the real angles, and then calculated the average and maximum values.

We compared the performance of the AVBM and IISU3EDGAN system in terms of rotor angle detection, as displayed in Figs. 16–19. According to the experimental results obtained for the left side of the rotor shaft in the first round of testing, the average angle deviation derived for the AVBM was 0.94°, and the maximum deviation was 1.7°; the average angle deviation derived for the IISU3EDGAN system was 0.7°, with the maximum deviation being 0.9°. For the right side of the rotor shaft, the average and maximum
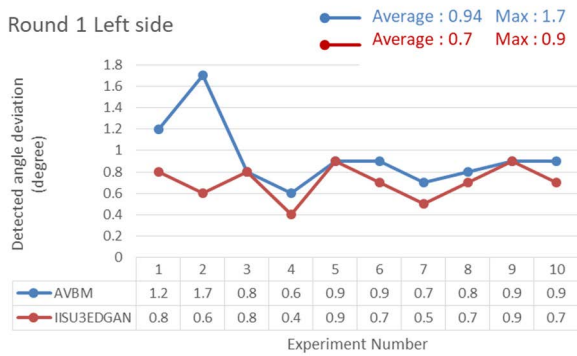
FIGURE 16. Comparison of detected angle deviations on left side of rotor shaft in Round 1.
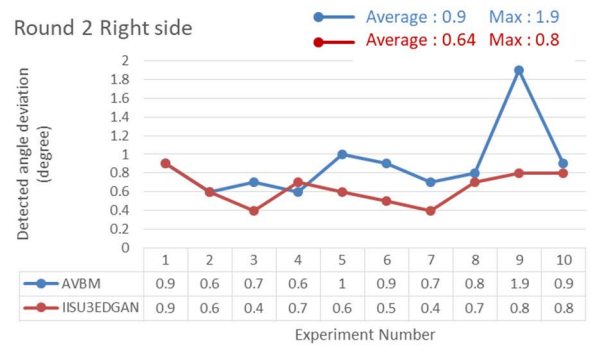

FIGURE 17. Comparison of detected angle deviations on right side of rotor shaft in Round 1.

FIGURE 18. Comparison of detected angle deviations on left side of rotor shaft in Round 2.

FIGURE 19. Comparison of detected angle deviations on right side of rotor shaft in Round 2.
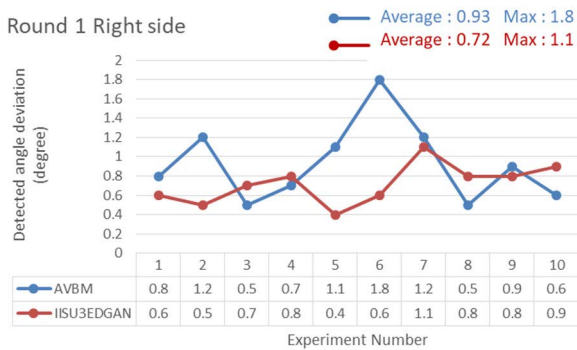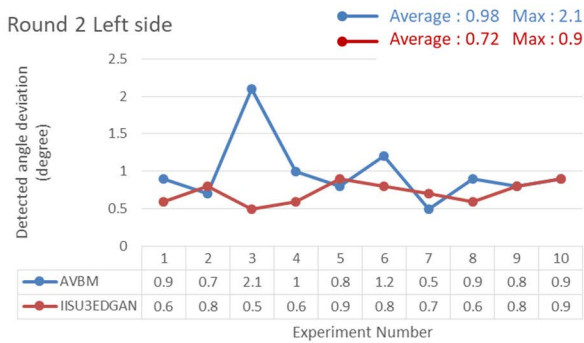
the rotor shaft, the average and maximum angle deviations derived for the AVBM were 0.9° and 1.9°, respectively, and those derived for the IISU3EDGAN system were 0.64° and 0.8°, respectively.

According to the preceding comparison results, the IISU3EDGAN system produced lower average and maximum angle deviations than did the AVBM. Therefore, the IISU3EDGAN system is effective for the inpainting of overexposed images of rotors of various sizes, and it can improve the accuracy of rotor angle detection.

C. PERFORMANCE EVALUATION

We selected two rotor models from each of the five size groups and then evaluated the dynamic balancing performance achieved using the IISU3EDGAN-repaired images by conducting two rounds of experiments. After generating the optimized dynamic balancing configurations, we compared the estimated results with the actual magnitude and angle of imbalance to determine the performance of our system. In each round of testing, dynamic balancing data were recorded for the left and right sides of the rotor shaft. Moreover, we recorded the deviations between the estimated and actual data, including the magnitude and angle of imbalance.

Tables 3 and 4 present a summary of the comparison between the estimated and actual magnitudes of imbalance after the completion of dynamic balancing. In the first round of testing, the average magnitudes of deviation for the left and right sides of the rotors were 0.461 g and 0.388 g, respectively, and the maximum magnitudes of deviation for these sides were 0.77 g and 0.69 g, respectively. In the second round, the average magnitudes of deviation for the left and right sides of the rotors were 0.472 g and 0.478 g, respectively, and the maximum magnitudes of deviation for these sides were 0.71 g and 0.78 g, respectively. Tables 5 and 6 present a comparison between the estimated and actual angles of imbalance after the completion of dynamic rotor balancing. In the first round of testing, the average deviation angles derived for the left and right sides of the rotors were 7.2° and 7.4°, respectively, and the maximum deviation angles derived

angle deviations derived for the AVBM were 0.93° and 1.8°, respectively, and those derived for the IISU3EDGAN system were 0.72° and 1.1°, respectively. In the second round of testing, we used the same test method. Regarding the test results obtained for the left side of the rotor shaft, the average and maximum angle deviations derived for the AVBM were 0.98° and 2.1°, respectively, and those derived for the IISU3EDGAN system were 0.72° and 0.9°, respectively. Regarding the test results obtained for the right side of

for these sides were 11° and 12°, respectively. In the second round, the average deviation angles derived for the left and right sides of the rotors were 7.4° and 7.3°, respectively, and the maximum deviation angles derived for these sides were 13° and 12°, respectively.

Fig. 20 summarizes the results obtained using the IISU3EDGAN system, including the detected angle deviations, magnitude deviations and angle deviations. It shows the 40 test data obtained for both the left and right sides of the rotor shafts in the two rounds of testing. Table 7 presents a comparison of the magnitude and angle deviations derived for the AVBM and IISU3EDGAN system. The average and maximum deviations obtained for the IISU3EDGAN system were smaller than those obtained for the AVBM. Therefore, the IISU3EDGAN system significantly improved the angle detection in the dynamic balancing of rotors.

Compared with the AVBM, the IISU3EDGAN system can be applied not only to a wider range of rotor weights but also to wider ranges of BS counts, washer limits, and washer weights. Moreover, it can be used to solve complex rotor overexposure problems and increase the accuracy of rotor angle detection. In terms of the overall production efficiency of rotor dynamic balancing, Table 8 presents a comparison of the number of rounds required by the dynamic balancing machine to balance a rotor by using different methods. In the first round, successful rotor dynamic balancing was achieved in 92% of the cases for the AVBM; for the proposed system, successful rotor dynamic balancing was achieved in 97% of the cases.

TABLE 3. Comparison of estimated and real magnitudes of rotor imbalance in round 1.

| Round 1 | Magnitude (g) | | | | | |
| | Estimated magnitude | | Real magnitude | | Magnitude deviation | |
Number	L	R	L	R	L	R
1	1.44	1.3	1.08	0.91	0.36	0.39
2	1.65	1.78	1.24	1.44	0.41	0.34
3	2.2	1.24	1.75	0.93	0.45	0.31
4	1.21	2.11	0.99	1.72	0.22	0.39
5	2.33	1.61	1.78	1.32	0.55	0.29
6	1.69	1.73	1.22	1.49	0.47	0.24
7	1.09	1.29	0.76	1.07	0.33	0.22
8	1.9	1.45	1.13	0.93	0.77	0.52
9	1.56	1.01	0.87	1.5	0.69	0.49
10	1.4	1.68	1.04	0.99	0.36	0.69
Average magnitude deviation					**0.461**	**0.388**
Max magnitude deviation					**0.77**	**0.69**

Table 9 presents a comparison of dynamic balancing times recorded for a manual method, the AVBM, and the IISU3EDGAN system. The manual method required three rounds to complete the dynamic balancing process, and the total dynamic balancing time was 184 s. The AVBM and proposed system required fewer rounds for balancing, and the total balancing times were 123 and 112 s, respectively. Compared with the manual method, the AVBM and proposed system reduced the dynamic balancing time by 33% and

TABLE 4. Comparison of estimated and real magnitudes of rotor imbalance in round 2.

| Round 2 | Magnitude (g) | | | | | |
| | Estimated magnitude | | Real magnitude | | Magnitude deviation | |
Number	L	R	L	R	L	R
1	1.43	2	0.98	1.37	0.45	0.63
2	1.79	1.98	1.22	1.34	0.57	0.64
3	1.5	1.51	1.29	1.23	0.21	0.28
4	1.81	1.89	1.25	1.32	0.56	0.57
5	1.59	1.74	1.12	0.96	0.47	0.78
6	1.99	1.57	1.78	1.31	0.21	0.26
7	2.09	2.44	1.51	1.77	0.58	0.67
8	1.34	1.7	0.98	1.47	0.36	0.23
9	2.03	0.95	1.32	0.8	0.71	0.15
10	2.36	2.06	1.76	1.49	0.6	0.57
Average magnitude deviation					**0.472**	**0.478**
Max magnitude deviation					**0.71**	**0.78**

TABLE 5. Comparison of estimated and real rotor imbalance angles in round 1.

| Round 1 | Angle (degree) | | | | | |
| | Estimated angle | | Real angle | | Angle deviation | |
Number	L	R	L	R	L	R
1	207	190	202	178	5	12
2	30	30	23	22	7	8
3	200	80	194	86	6	6
4	115	53	122	49	7	4
5	103	297	92	292	11	5
6	127	218	118	228	9	10
7	195	258	189	267	6	9
8	158	330	168	339	10	9
9	230	31	235	24	5	7
10	165	15	171	11	6	4
Average angle deviation					**7.2**	**7.4**
Max angel deviation					**11**	**12**

TABLE 6. Comparison of estimated and real rotor imbalance angles in round 2.

| Round 2 | Angle (degree) | | | | | |
| | Estimated angle | | Real angle | | Angle deviation | |
Number	L	R	L	R	L	R
1	215	66	220	60	5	6
2	175	147	183	141	8	6
3	211	325	205	334	6	9
4	291	303	282	298	9	5
5	280	7	287	15	7	8
6	190	309	196	314	6	5
7	182	202	174	190	8	12
8	102	238	96	244	6	6
9	285	195	298	199	13	4
10	245	325	251	337	6	12
Average angle deviation					**7.4**	**7.3**
Max angel deviation					**13**	**12**

39%, respectively. In other words, the IISU3EDGAN system not only effectively reduced the dynamic balancing time but also outperformed the AVBM in terms of image restoration. Considering the overall rotor dynamic balancing process, we compared the processing times required by the manual method, AVBM, and proposed system, as listed in Table 10. The total processing time required by the manual method was
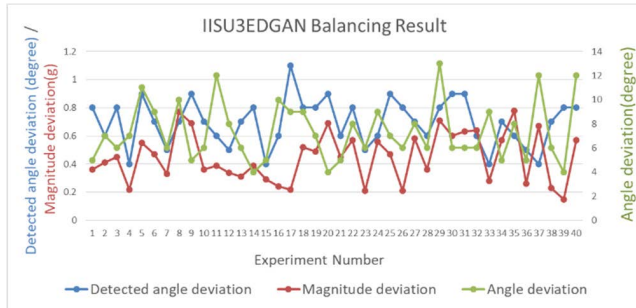
FIGURE 20. IISU3EDGAN balancing results.

TABLE 7. Comparison of imbalance data between the AVBM and IISU3EDGAN methods.

Round		Magnitude deviation (g)				Angle deviation (degree)			
		Average		Max		Average		Max	
		AVBM	Ours	AVBM	Ours	AVBM	Ours	AVBM	Ours
1	L	0.512	**0.461**	0.93	**0.77**	9.2	**7.2**	15	**11**
	R	0.533	**0.388**	0.95	**0.69**	8.9	**7.4**	19	**12**
2	L	0.59	**0.472**	1.1	**0.71**	10.1	**7.4**	17	**13**
	R	0.571	**0.478**	0.97	**0.78**	9.7	**7.3**	20	**12**

TABLE 8. Number of rounds required to complete balancing.

Round	Rotor counts		Percentage (%)	
	AVBM	IISU3EDGAN	AVBM	IISU3EDGAN
First	184	192	**92**	**97**
Second	16	8	8	3
Total	200	200	100	100
First round improvement				**5%**

TABLE 9. Comparison of time required for machine balancing.

Process	Item	Time (sec)		
		Manual	AVBM	IISU3EDGAN
Machine balancing	Balancing round	115	51	40
	Visual recognition	0	3	3
	Place and confirm	69	69	69
Total time (sec)		**184**	**123**	**112**
Time improvement			**33%**	**39%**

TABLE 10. Comparison of rotor balancing operation times.

Process	Item	Time (sec)		
		Manual	AVBM	IISU3EDGAN
Rotor dynamic balancing	Loading	8.1	8.1	8.1
	Machine balancing	184	123	112
	Unloading	7.6	7.6	7.6
	Others	21.2	21.2	21.2
	Transporting	138	138	138
Total operation time		**358.9**	**297.9**	**286.9**
Production per day		**80**	**97**	**100**
Production improvement			**21%**	**25%**

358.9 s, whereas the processing times required by the AVBM and proposed system were 297.9 and 286.9 s, respectively. For an 8-h working day, the numbers of rotors processed by the manual method, AVBM, and proposed system could be estimated be 80, 97, and 100, respectively. Thus, the AVBM and the proposed IISU3EDGAN system could increase the number of rotors produced by 21% and 25%, respectively. Overall, the IISU3EDGAN system could effectively increase rotor production by 25%, and it was determined to be superior to the AVBM. Therefore, the IISU3EDGAN system has extensive applicability and a considerably high detection accuracy, and it can improve overall rotor productivity.

V. CONCLUSION

We developed an IISU3EDGAN system based on a 3D-ED-GAN for performing 3D image inpainting to achieve efficient vision-based detection for rotor dynamic balancing. The system can reconstruct overexposed 3D rotor images while retaining their detailed features. The system also exhibits improved detection accuracy for the angles of rotor components, which can increase the overall rotor dynamic balancing performance. The main contribution of this study is the integration and development of deep learning and GAN-based methods for 3D image inpainting. In practical industrial applications, the proposed IISU3EDGAN system can solve the complex problem of inpainting overexposed images caused by differences in rotor types on a production line. Compared with the AVBM, which uses traditional image processing methods for image restoration, the proposed IISU3EDGAN system can be applied to more diverse types of rotors in terms of rotor weight, BS count, washer limit, and washer weight. Moreover, it is more accurate in terms of rotor component detection. The IISU3EDGAN system also reduces the number of rounds required for rotor balancing, thus improving production efficiency. The system was noted to improve the balancing time by 5% compared with the AVBM. In a comparison of a manual method and the IISU3EDGAN system, we observed that the proposed system improved the rotor balancing time and the overall rotor production by 39% and 25%, respectively. Accordingly, we conclude that the proposed IISU3EDGAN system for rotor dynamic balancing improves production efficiency on actual production lines. Notably, the effectiveness of the IISU3EDGAN system was confirmed by Taiwan-based manufacturers who use rotor dynamic balancing machines.

REFERENCES

[1] *International Organization of Standardization, Mechanical Vibration Balance Quality Requirements for Rotors in a Constant (Rigid) State—Part 1: Specification and Verification of Balance Tolerances*, Standard ISO 1940-1:2003, 2003.

[2] W. C. Foiles, P. E. Allaire, and E. J. Gunter, "Rotor balancing," *Shock. Vib.*, vol. 5, no. 5, 6, pp. 325–336, Jan. 1998.

[3] M. MacCamhaoil, "Static and dynamic balancing of rigid rotors," Bruel & Kjaer, Nærum, Denmark, Appl. Notes, BO 0276-12, 2016.

[4] P. Diouf and W. Herbert, "Understanding rotor balance for electric motors," in *Proc. Conf. Rec. Annu. Pulp Paper Ind. Tech. Conf.*, Jun. 2014, pp. 7–17, doi: 10.1109/PPIC.2014.6871143.

[5] F. Fujisawa, T. Kojima, T. Terayama, K. Shiohata, and H. Yokota, "Balancing method for a rigid rotor considering constraint of the correction mass," *Trans. Jpn. Soc. Mech. Eng., C*, vol. 59, no. 558, pp. 78–83, 1993.

[6] S. Zhang, Y. Wang, and Z. Zhang, "Online dynamic balance technology for high speed spindle based on gain parameter adaption and scheduling control," *Appl. Sci.*, vol. 8, no. 6, p. 917, Jun. 2018.

[7] S. Zhao, X. Ren, W. Deng, K. Lu, Y. Yang, and C. Fu, "A transient characteristic-based balancing method of rotor system without trail weights," *Mech. Syst. Sig. Process.*, vol. 148, Feb. 2021, Art. no. 107117.

[8] K. Green, A. R. Champneys, and N. J. Lieven, "Bifurcation analysis of an automatic dynamic balancing mechanism for eccentric rotors," *J. Sound Vibrat.*, vol. 291, nos. 3–5, pp. 861–881, Apr. 2006.

[9] Z. Kai and Z. Xiaozhang, "Rotor dynamic balance making use of adaptive unbalance control of active magnetic bearings," in *Proc. Int. Conf. Intell. Syst. Design Eng. Appl.*, Oct. 2010, pp. 347–350, doi: 10.1109/ISDEA.2010.377.

[10] S. Liu and L. Qu, "A new field balancing method of rotor systems based on holospectrum and genetic algorithm," *Appl. Soft Comput.*, vol. 8, no. 1, pp. 446–455, Jan. 2008.

[11] S. Ostlund and M. Brokemper, "Sensorless rotor-position detection from zero to rated speed for an integrated PM synchronous motor drive," *IEEE Trans. Ind. Appl.*, vol. 32, no. 5, pp. 1158–1165, Sep. 1996, doi: 10.1109/28.536878.

[12] P. B. Schmidt, M. L. Gasperi, C. Ray, and A. H. Wijenayake, "Initial rotor angle detection of a nonsalient pole permanent magnet synchronous machine," in *Proc. Conf. Rec. IEEE Ind. Appl. Conf. 32nd IAS Annu. Meeting (IAS)*, vol. 1, Oct. 1997, pp. 459–463, doi: 10.1109/IAS.1997.643063.

[13] P. L. Jansen and R. D. Lorenz, "Transducerless position and velocity estimation in induction and salient AC machines," *IEEE Trans. Ind. Appl.*, vol. 31, no. 2, pp. 240–247, Mar. 1995, doi: 10.1109/28.370269.

[14] M. W. Degner and R. D. Lorenz, "Using multiple saliencies for the estimation of flux, position, and velocity in AC machines," *IEEE Trans. Ind. Appl.*, vol. 34, no. 5, pp. 1097–1104, Sep. 1998, doi: 10.1109/28.720450.

[15] Y.-H. Chung, C.-W. Yu, B.-R. Wen, and Y.-L. Chen, "Automatic adjustment method for rotor dynamic balance system," in *Proc. Int. Symp. Comput., Consum. Control (IS3C)*, Nov. 2020, pp. 61–64, doi: 10.1109/IS3C50286.2020.00023.

[16] Y.-H. Chung and Y.-L. Chen, "Adaptive vision-based method for rotor dynamic balance system," *IEEE Access*, vol. 9, pp. 22996–23006, 2021, doi: 10.1109/ACCESS.2021.3055257.

[17] M. Hansard, S. Lee, O. Choi, and R. Horaud, *Time-of-Flight Cameras: Principles, Methods and Applications* (Brief in Computer Science). London, U.K.: Springer, 2012.

[18] H. Yu, K. Zhao, Y. Wang, L. Kan, M. Sun, and W. Jia, "Registration and fusion for ToF camera and 2D camera reading," in *Proc. Chin. Autom. Congr.*, Nov. 2013, pp. 679–684, doi: 10.1109/CAC.2013.6775821.

[19] L. Li, "Time-of-flight camera—An introduction," Texas Instrum., Dallas, TX, USA, White Paper SLOA190B, 2014.

[20] D. Guo, Y. Cheng, S. Zhuo, and T. Sim, "Correcting over-exposure in photographs," in *Proc. IEEE Comput. Soc. Conf. Comput. Vis. Pattern Recognit.*, Jun. 2010, pp. 515–521, doi: 10.1109/CVPR.2010.5540170.

[21] D.-H. Lee, Y.-J. Yoon, S.-J. Kang, and S.-J. Ko, "Correction of the overexposed region in digital color image," *IEEE Trans. Consum. Electron.*, vol. 60, no. 2, pp. 173–178, May 2014, doi: 10.1109/TCE.2014.6851990.

[22] Q. Zhang, Y. Nie, and W. Zheng, "Dual illumination estimation for robust exposure correction," *Comput. Graph. Forum*, vol. 38, no. 7, pp. 243–252, Oct. 2019.

[23] X. Huang, Y. Xia, L. Shi, Y. Huang, M. Yan, J. Hornegger, and A. Maier, "Mixed one-bit compressive sensing with applications to overexposure correction for CT reconstruction," 2017, *arXiv:1701.00694*.

[24] Y.-H. Chung, C.-W. Yu, B.-R. Wen, and Y.-L. Chen, "Depth information based image restoration method for rotors," in *Proc. IEEE Int. Conf. Consum. Electronics-Taiwan (ICCE-TW)*, Sep. 2021, pp. 1–2, doi: 10.1109/ICCE-TW52618.2021.9602981.

[25] I. Goodfellow, J. Pouget-Abadie, M. Mirza, B. Xu, D. Warde-Farley, S. Ozair, A. Courville, and Y. Bengio, "Generative adversarial nets," in *Proc. Adv. Neural Inf. Process. Syst.*, 2014, pp. 2672–2680.

[26] E. Denton, S. Chintala, A. Szlam, and R. Fergus, "Deep generative image models using a Laplacian pyramid of adversarial networks," 2015, *arXiv:1506.05751*.

[27] A. Radford, L. Metz, and S. Chintala, "Unsupervised representation learning with deep convolutional generative adversarial networks," 2015, *arXiv:1511.06434*.

[28] A. X. Chang, T. Funkhouser, L. Guibas, P. Hanrahan, Q. Huang, Z. Li, S. Savarese, M. Savva, S. Song, H. Su, J. Xiao, L. Yi, and F. Yu, "ShapeNet: An information-rich 3D model repository," 2015, *arXiv:1512.03012*.

[29] Z. Wu, S. Song, A. Khosla, F. Yu, L. Zhang, X. Tang, and J. Xiao, "3D ShapeNets: A deep representation for volumetric shapes," in *Proc. IEEE Conf. Comput. Vis. Pattern Recognit. (CVPR)*, Jun. 2015, pp. 1912–1920, doi: 10.1109/CVPR.2015.7298801.

[30] P. Achlioptas, O. Diamanti, I. Mitliagkas, and L. J. Guibas, "Learning representations and generative models for 3D point clouds," in *Proc. Int. Conf. Mach. Learn.*, 2018, pp. 40–49.

[31] D. Valsesia, G. Fracastoro, and E. Magli, "Learning localized generative models for 3D point clouds via graph convolution," in *Proc. Int. Conf. Learn. Represent.*, 2019, pp. 1–15.

[32] X. Yan, J. Yang, E. Yumer, Y. Guo, and H. Lee, "Perspective transformer nets: Learning single-view 3D object reconstruction without 3d supervision," in *Proc. 30th Int. Conf. Neural Inf. Process. Syst. (NIPS)*, 2016, pp. 1696–1704.

[33] R. Girdhar, D. F. Fouhey, M. Rodriguez, and A. Gupta, "Learning a predictable and generative vector representation for objects," in *Proc. Eur. Conf. Comput. Vis. (ECCV)*, Oct. 2016, pp. 484–499.

[34] M. Wei, J. Wu, and M. Pang, "An integrated approach to filling holes in meshes," in *Proc. Int. Conf. Artif. Intell. Comput. Intell.*, Oct. 2010, pp. 306–310.

[35] D. Pathak, P. Krahenbuhl, J. Donahue, T. Darrell, and A. A. Efros, "Context encoders: Feature learning by inpainting," in *Proc. IEEE Conf. Comput. Vis. Pattern Recognit. (CVPR)*, Jun. 2016, pp. 2536–2544.

[36] X. Wang, D. Xu, and F. Gu, "3D model inpainting based on 3D deep convolutional generative adversarial network," *IEEE Access*, vol. 8, pp. 170355–170363, 2020, doi: 10.1109/ACCESS.2020.3024288.

[37] A. Dai, C. R. Qi, and M. NieBner, "Shape completion using 3D-encoder-predictor CNNs and shape synthesis," in *Proc. IEEE Conf. Comput. Vis. Pattern Recognit. (CVPR)*, Jul. 2017, pp. 6545–6554, doi: 10.1109/CVPR.2017.693.

[38] Y. Yu, Z. Huang, F. Li, H. Zhang, and X. Le, "Point encoder GAN: A deep learning model for 3D point cloud inpainting," *Neurocomputing*, vol. 384, pp. 192–199, Apr. 2020.

[39] J. Kossaifi, A. Bulat, G. Tzimiropoulos, and M. Pantic, "T-Net: Parametrizing fully convolutional nets with a single high-order tensor," in *Proc. IEEE/CVF Conf. Comput. Vis. Pattern Recognit. (CVPR)*, Jun. 2019, pp. 7814–7823, doi: 10.1109/CVPR.2019.00801.

[40] B. Yang, H. Wen, S. Wang, R. Clark, A. Markham, and N. Trigoni, "3D object reconstruction from a single depth view with adversarial learning," in *Proc. IEEE Int. Conf. Comput. Vis. Workshops (ICCVW)*, Oct. 2017, pp. 679–688, doi: 10.1109/ICCVW.2017.86.

[41] W. Wang, Q. Huang, S. You, C. Yang, and U. Neumann, "Shape inpainting using 3D generative adversarial network and recurrent convolutional networks," in *Proc. IEEE Int. Conf. Comput. Vis. (ICCV)*, Oct. 2017, pp. 2317–2325, doi: 10.1109/ICCV.2017.252.

[42] Y.-H. Chung and Y.-L. Chen, "3D image inpainting for rotor detection using 3D encoder–decoder generative adversarial network," in *Proc. IEEE Int. Symp. Product Compliance Eng. Asia (ISPCE-ASIA)*, Nov. 2021, pp. 1–2, doi: 10.1109/ISPCE-ASIA53453.2021.9652180.

[43] *TECO*. teco.com.tw. Accessed: Jan. 31, 2022. [Online]. Available: https://www.teco.com.tw/en

[44] *Balancing Machine, Dynamic Balancing Machine Nan Jung Electronic Co., Ltd*. Balancingmachine.com. Accessed: Jan. 31, 2022. [Online]. Available: https://www.balancingmachine.com/en/

[45] *FocusVision Technology 3D Imaging and Sensing*. Focusvision.Tech. Accessed: Jan. 31, 2022. [Online]. Available: https://www.focusvision.tech

[46] J. Donahue, P. Krähenbühl, and T. Darrell, "Adversarial feature learning," 2016, *arXiv:1605.09782*.

YI-HAO CHUNG received the B.S. and M.S. degrees in computer science and information engineering from Tamkang University, Tamsui, Taiwan, in 1997 and 1999, respectively. He is currently pursuing the Ph.D. degree in computer science and information engineering with the National Taipei University of Technology, Taipei, Taiwan. His research interests include computer vision, artificial intelligence, sensor fusion, image processing, intelligent system integration, and 3D sensor calibration.

YEN-LIN CHEN (Senior Member, IEEE) received the B.S. and Ph.D. degrees in electrical and control engineering from the National Chiao Tung University, Hsinchu, Taiwan, in 2000 and 2006, respectively. From February 2007 to July 2009, he was an Assistant Professor at the Department of Computer Science and Information Engineering, Asia University, Taichung, Taiwan. From August 2009 to January 2012, he was an Assistant Professor and from February 2012 to July 2015, he was an Associate Professor at the Department of Computer Science and Information Engineering, National Taipei University of Technology, Taipei, Taiwan, where he has been a Full Professor, since August 2015. His research interests include artificial intelligence, intelligent image analytics, embedded systems, pattern recognition, intelligent vehicles, and intelligent transportation systems. His research results have been published on over 150 journals and conference papers. He is a fellow of IET and a member of ACM, IAPR, and IEICE.

. . .